An Electrothermal and Magnetic Dual-Modal Actuator toward Soft Self-Sensing Robots

Quan Shu, Guojiang Liao, Shuai Liu, Huaxia Deng, Haoming Pang, Zhenbang Xu, Xinglong Gong,* and Shouhu Xuan

Soft actuators with good flexibility, high stability, and excellent controllability have attracted extensive attention. However, dual-modal smart self-perception actuator with contact and noncontact actuating mode remains a challenge. Notably, soft actuators with in situ self-sensing monitoring capabilities have gained increasing attention in smart flexible devices. This work reports a smart actuator composed of polydimethylsiloxane (PDMS)/ magnetorheological elastomer (MRE)/Ag/ polyimide (PI) (PMAP), which can not only well respond to bending stimuli but also be actuated by electromagnetic dual-modal actuation. Benefiting from the nanowire–nanoflake coupling structure of conductive Ag layer, the PMAP film exhibits excellent electrical sensing and electro-heat generation behavior. The $\Delta R/R_0$ of PMAP film increases from 5.1% to 24.7% during the bending test. Moreover, the PMAP film realizes contact electrothermal actuation due to the mismatch of thermal expansion coefficient between PDMS matrix and PI tape. Under applying a 16 s of 2 V electrothermal actuation, the bending angle of PMAP film can increase from 31.1° to 219.3°. Moreover, MRE matrix endows the PMAP film with noncontact magnetic deformation characteristic. This multifunctional smart flexible device integrated with in situ sensing perception and contact and noncontact dual-modal actuation performances possess high potential in electronic devices and robots.

1. Introduction

During the past decade, varieties of high-performance flexible sensor with thin film structure, multilayer structure, fibrous structure, and 3D geometry structure have been successfully constructed.[1] Typically, flexible sensor with thin film structure based on polydimethylsiloxane (PDMS) matrix can respond well to the contact external stimuli (such as bending and compression).[2–7] Wang et al. reported a film sensor based on PDMS matrix with good electrical response to pressure and bending detection.[8] More notably, Sang et al. presented the next-generation smart devices should possess multifunctionalities to meet the external requirements because of the complicated application environment.[9] Therefore, flexible sensors with sensing-actuating coupling performance received extensive attention.[10–15] It was reported that a flexible sensor based on magnetorheological elastomer (MRE) matrix endowed the electronics with magnetic actuating and magnetic/stress coupling sensing capabilities.[16] However, the multifunctional and diversification smart actuators with contact sensing detection are still scarce. Hence, the construction of intelligent flexible materials with multimodal actuation and in situ sensing is important for the development of soft actuators.

Because the soft actuators can spontaneously convert the external stimuli such as electricity, light, humidity and magnetic field into mechanical deformation, they show promising applications in soft robotics, aerospace engineering and intelligent artificial muscles.[9] The traditional soft material actuators were mainly actuated by single mode, such as electric,[17–19] magnetic,[20–22] and thermal[23–25] actuation. Dai et al. proposed a soft magnetic actuator with bionic sandwich structure, and this work focused on designing highly deformable actuators and functions in emerging areas of soft robotics.[26] Recently, Jiang et al. developed a soft actuator based on the mismatch of thermal expansion of the PDMS and polyimide (PI) layers upon the application of thermal energy through Joule heating.[27] However, due to the complicated application environment, the single mode actuators limit their practical application in specific situations. In order to further improve

Q. Shu, S. Liu, H. Deng, H. Pang, X. Gong, S. Xuan
CAS Key Laboratory of Mechanical Behavior and Design of Materials
Department of Modern Mechanics
University of Science and Technology of China
Hefei, Anhui 230027, P. R. China
E-mail: gongxl@ustc.edu.cn
G. Liao
Science and Technology on Reactor System Design Technology
Laboratory
Nuclear Power Institute of China
Chengdu, Sichuan 610041, P. R. China
Z. Xu
CAS Key Laboratory of On-orbit Manufacturing and Integration for Space
Optics System
Changchun Institute of Optics
Fine Mechanics and Physics
Chinese Academy of Sciences
Changchun 130033, P. R. China

**ADVANCED
SCIENCE NEWS**

www.advancedsciencenews.com

**ADVANCED
MATERIALS
TECHNOLOGIES**

www.advmattechnol.de

the actuating efficiency and controllability of intelligent soft material actuators, dual-modal flexible actuator provides a new idea for the design of high-performance smart electronics.[28] For example, Li et al. fabricated a dual-modal soft actuator with electrothermal/magnetic coupling actuation characteristics, which was successfully applied in the smart crawling robots.[28] Nevertheless, it is still difficult for the controlling system of the soft actuators to directly catching the actuating states during the dual-modal actuation. Therefore, the construction of contact and noncontact dual-modal soft actuate devices with sensing function has become an urgent problem.

A typical soft electrothermal actuator is composed of two polymer layers with different thermal expansion coefficient and a pivotal conductive layer,[9] in which the conductive layer plays a key role in determining both the sensing and actuation performance. Sliver nanowires (AgNWs) show excellent conductivity and sensitivity, which are widely used in flexible sensor,[29–31] electronic skin,[32–34] electrothermal actuate.[27] Gao et al. proposed a flexible conductive membrane based on AgNWs and believed it was a good candidate for smart devices and soft robots.[35] Notably, silver (Ag) flake is a high-purity and high conductivity material, which shows a stable 2D sheet laminar structure and superb electrothermal effect.[36] It is reported that high-performance actuators should meet the requirements of low actuation voltage, large deformation, and low resistance.[27,28] Hence, a 3D conductive structure can be formed by combining the 1D linear structure of AgNWs with the 2D sheet laminar structure of Ag flake, which greatly enhances the conductivity and reduces the resistance. Obviously, tuning the assembling nanostructure of the Ag conductive layer must be an effectively method to construct high-performance electronic devices. The AgNWs presents good sensing performance,[30,31] while the bulk conductor is beneficial for improving the conductivity. Therefore, it is important to study the combination of Ag nanowire and nanoflake for designing actuation systems with unique sensing and electrothermal actuate behaviors.

Herein, a smart soft film composed of PDMS/MRE/Ag layer/PI (PMAP) with dual-modal actuation is fabricated. The bending and compression mechanical stimuli of PMAP film can be responded with sensing electric signal. Notably, the conductive Ag layer shows good electrification heat generation characteristic. The difference of thermal expansion coefficient between PDMS matrix and PI tape endows PMAP with electrothermal actuating behavior, and the contact actuating working mode is realized. Additionally, the noncontact magnetic actuate mode of PMAP film is also originated from the inherent magnetic matrix. Therefore, a biomimetic Venus flytrap can be further developed based on the PMAP film due to its wonderful magnetic and electrothermal bimodal actuation. This PMAP film can be employed as a multifunctional intelligent actuator with contact sensing performance integration because of its good electrical and stimuli-responsiveness characteristics.

2. Results and Discussion

2.1. Preparation and Characterization of PMAP

Figure 1a depicts the schematic preparation process of PMAP actuator with high conductivity and good stability characteristics. Here, the conductive Ag layer endows PMAP film with good electro-heat behavior (Figure 1b). Moreover, the PMAP film can also be used as a sensor by changing the resistance of conductive Ag layer under the external stimuli. Notably, the MRE matrix endow the PMAP film with excellent magnetic actuate performance. Interestingly, the Ag layer can monitor the magnetic actuate in real time and feedback the deformation with instant sensing signal. Therefore, the PMAP film shows the contact electrothermal actuation and noncontact magnetic actuation behavior with self-sensing characteristic. The XPS spectra were employed to analyze the chemical element of AgNWs and Ag layer (Figure 1c). As shown in Figure 1c, the tiny O 1s and C 1s peaks were shown in the spectra of the AgNWs and Ag layer. Notably, the AgNWs was self-prepared, form a solution which contained $AgNO_3$, NaCl, Polyvinylpyrrolidone (PVP, $(C_6H_9NO)_n$) and glycerol ($C_3H_8O_3$). The residue PVP and glycerol which adsorbed on the surface of the final AgNWs contain a large number of C and O atoms, so the O and C peaks were detected in the XPS spectra of AgNWs. Moreover, the Ag layer was consisted of the AgNWs and Ag flakes, and then the O 1s and C 1s peaks can also be detected. The strong peaks of Ag 3d were clearly found in the spectra of the AgNWs and Ag layer due to the high silver content in the conductive mixture. The 3D conductive structures formed by ultrasonically mixing AgNWs rod-like structures and Ag flake 2D structures. As shown in the XRD, the sharp peaks of Ag flake and AgNWs can be indexed to be the Ag crystalline phrase, which presents the nano-structure of Ag and ensures the good connection between the Ag nanowire and nanoflake (Figure 1d).

Here, Figure 1e shows the optical images of Ag flake i), AgNWs solution ii), PDMS/MRE/Ag layer iii), and microscope optical image of Ag layer iv). The Ag layer with a simple square coating structure was prepared to investigate the sensing performance (Figure 1eiii). Figure 1eiv shows the Ag flake and AgNWs form a dense conductive Ag layer, and thus exhibit stable conductivity. The SEM image of Ag layer indicates the 3D staggered structure are formed by AgNWs and Ag flakes (Figure 1f). The elemental mapping images of Figure 1f are presented in Figure 1g,h, which disclose the element composition and spatial distribution. Clearly, Ag, C, O, and Si elements are evenly distributed throughout the Ag layer, which demonstrate the stable 3D staggered conductive structure of the final product. Therefore, the Ag layer enables good sensitivity of the sensor and excellent conductivity of the actuator.

2.2. Mechanic–Electric Coupling Behavior of the PMAP

Due to the high tensile characteristic of PI, the Ag layer combined with MRE matrix showed high flexibility and thus PMAP film can be applied as the bending sensor. The bending and compression stimulation responsive performances of PMAP film were investigated by using an electroforce system and an electrical property test system Modulab MTS (**Figure 2**; Figure S2, Supporting Information). The behaviors of the bending displacement, loading signal waveforms and frequencies, multicycle stability and sensitivity were systematically performed and researched. Figure 2ai shows the image of PMAP film under bending excitation. Clearly, the optical microscope image exhibits that the conductive Ag layer shows obvious cracks under
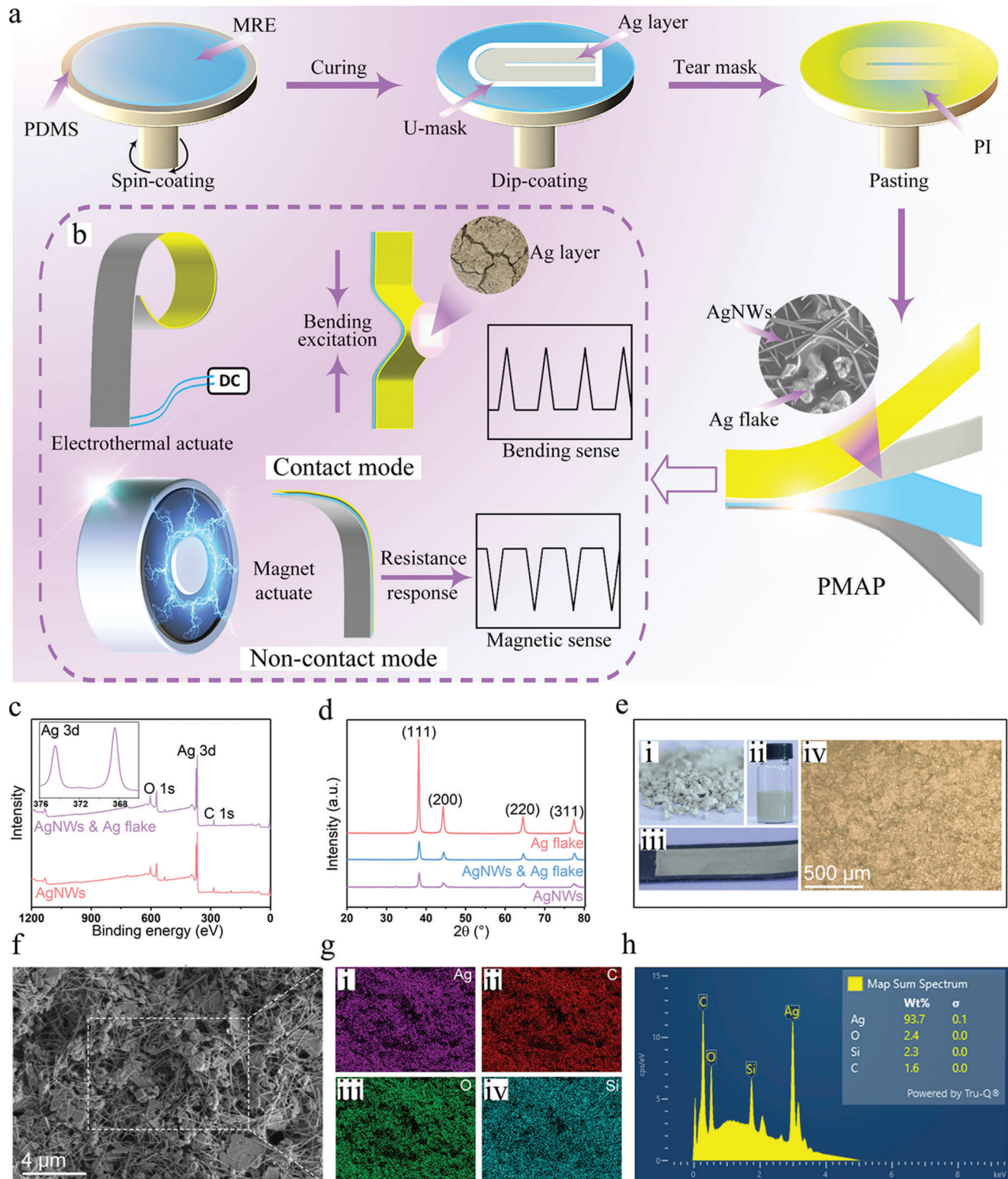
Figure 1. Preparation process of a) PMAP and b) the potential application of PMAP actuator in electrothermal actuate and noncontact magnetic actuate; c) XPS patterns of AgNWs and Ag layer; d) XRD patterns of AgNWs, Ag flake and Ag layer; e) the images of i) Ag flake, ii) AgNWs solution, iii) PDMS/MRE/Ag layer, and iv) optical microscope image of Ag layer; f) SEM image of Ag layer, g) energy-dispersive X-ray spectroscopy element mappings, and h) element analysis of Ag layer.
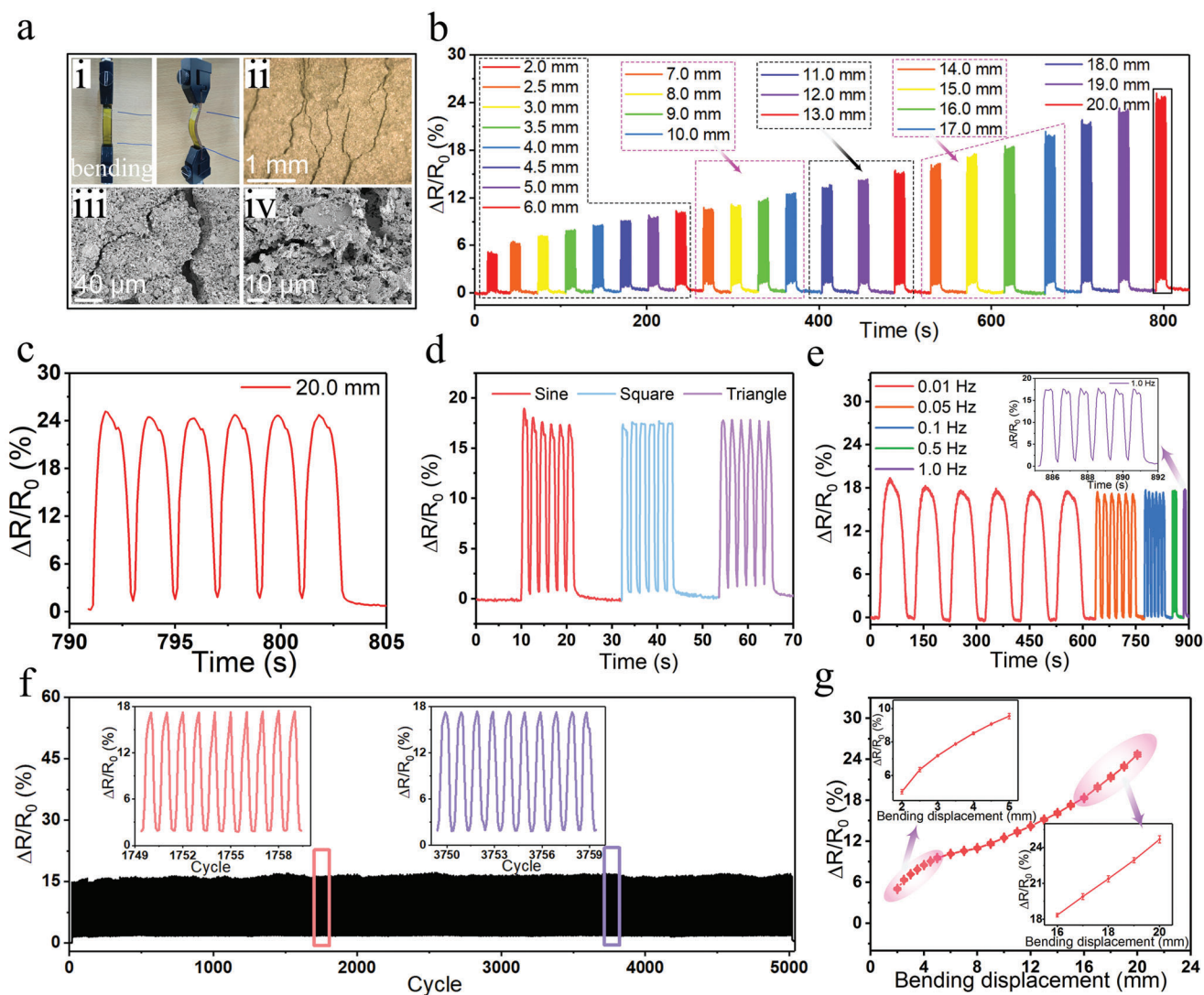
**ADVANCED
SCIENCE NEWS**

www.advancedsciencenews.com

**ADVANCED
MATERIALS
TECHNOLOGIES**

www.advmattechnol.de

Figure 2. a) i) Sensing performance of PMAP under bending loading, ii) optical microscope image of Ag layer, and iii,iv) SEM images of Ag layer and the enlarged area; b) Bending sensing performance with different bending displacement at frequency of 0.5 Hz; c) Magnified curve of $\Delta R/R_0$ under the bending displacement of 20 mm; d) different waveforms of electrical performance at displacement of 15 mm; e) real-time $\Delta R/R_0$ response with different frequencies; f) the stability under 5000 cycles bending; g) $\Delta R/R_0$ versus bending displacement. Inset: The enlarged area of $\Delta R/R_0$ versus bending displacement.

bending excitation (Figure 2aii). Moreover, the SEM images of Figure 2aiii and the enlarged image of Figure 2aiv present the Ag layer was deformed, the microstructure was damaged, and the cracks were formed. Notably, the Ag mixture was still interconnected and thus ensured the conductivity of PMAP film. As shown in Figure 2b, the applied bending displacement varied from 2 mm to as high as 20 mm at 0.5 Hz loading frequency, and the $\Delta R/R_0$ of PMAP film increased from 5.1% to 24.7%. Obviously, $\Delta R/R_0$ increases with increasing of the bending displacement. Here, the PMAP film shows good stability and conductivity throughout the bending deformation stage.

By keeping the bending displacement at 20 mm, the cyclic loading was performed for six cycles, and the $\Delta R/R_0$ almost kept at a constant value (Figure 2c). Furthermore, the bending displacement was set at 15 mm to investigate its sensing performance under different loading waveforms of sine, triangular, and square waves (Figure 2d). The resistance responses of PMAP were consistent, and different loading waveforms of bending could be well responded by the film. When the frequencies were varied from 0.01 to 1 Hz, the electrical responses of PMAP were similar (Figure 2e). Therefore, the loading frequency showed few influence on the sensing perception behavior of PMAP. Moreover, by keeping 0.5 Hz frequency and 15 mm bending displacement as constant, the robustness of PMAP under 5000 loading cycles were tested (Figure 2f). After 1750 cycles of bending excitation, the $\Delta R/R_0$ of PMAP was 17.2%. Moreover, after 3750 cycles, the $\Delta R/R_0$ of PMAP changed to 17.3%. Therefore, the PMAP film shows a good durability and stability.

Figure 2g shows the sensing property of the PMAP by analyzing the relationship of $\Delta R/R_0$ and bending displacement (from
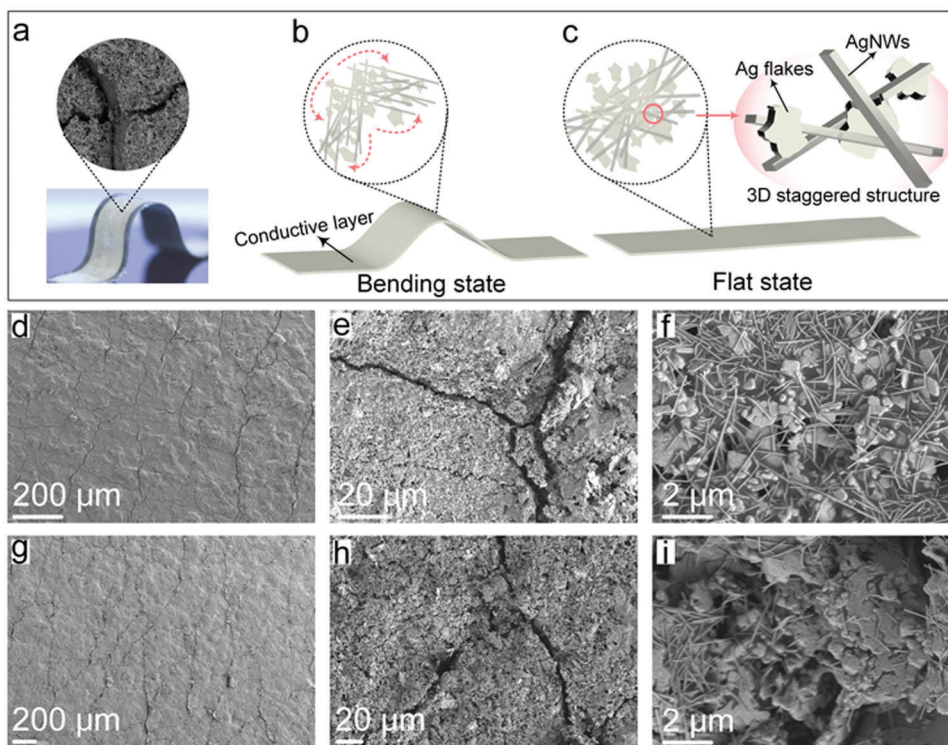
Figure 3. a) The SEM and optical images of Ag layer under bending loading; the microstructure schematic diagram of Ag layer under b) bending loading state and c) without loading state; SEM images of d) Ag layer after 200 bending loading–unloading cycles, e) the enlarged area of the cracks between the Ag layer, and f) magnified view of Ag mixture; SEM images of g) Ag layer after 5000 bending loading–unloading cycles, h) the enlarged area of the cracks between the Ag layer, and i) magnified view of Ag mixture.

2 mm to 20 mm). The sensitivity coefficients are approximated to three response ranges, and the corresponding bending displacement was divided into 2–5 mm (the first range), 6–15 mm, and 16–20 mm (the third range), respectively. The insets of Figure 2g exhibit enlarged view of the first range and the third range, respectively. Here, the gauge factor (GF) is defined as $(\Delta R/R_0)/\Delta l$, where the Δl represents relative bending displacement change. In the first range, the GF of PMAP is 0.8% mm^{-1}. As the bending displacement increased from 16 to 20 mm, the $\Delta R/R_0$ increased from 18.2% to 24.7%. In the third range, the GF of PMAP is calculated at 1.63% mm^{-1}. Clearly, the sensitivity gradually increases with increasing of the bending displacement. As a result, the PMAP film exhibits excellent stability and good sensitivity during the bending process.

In order to further investigate the electrical response mechanism of the conductive layer, the microstructure changes of Ag layer after bending loading–unloading was deeply researched (**Figure 3**). In Figure 3a, the optical image shows the Ag layer under bending loading state, and SEM image exhibits the crack defect caused by external mechanical stimulation. Here, the AgNWs and Ag flake schematic diagram under bending loading was used to depict the axial extrusion traction effect of the Ag mixture (Figure 3b). Under bending, the conductive network between the AgNWs and Ag flake was damaged, resulting in a decrease in the contact node and eventually leading to an increase in resistance. The schematic diagram of Figure 3c shows the conductive microstructure of Ag layer without bending load. Notably, the 3D structure between the AgNWs and Ag flake of conductive layer

was maintained without external mechanical stimulation. The staggered stacking structure and interaction of the Ag mixture endow the PMAP film with excellent and stable conductivity.

Figure 3d,g presents the SEM images of the Ag layer after 200 cycles and 5000 cycles, respectively. Clearly, the cracks in the conductive layer were formed under bending stimulation. Figure 3e shows the enlarged area of the cracks, which are responsible for the periodic rise in resistance during the cyclic loading experiments. After 200 bending cycles, the Ag nanowire and nanoflake remains connected to each other among the cracks, which endows the conductive layer with the ability to reduce the resistance to the initial value after the external mechanic unloading (Figure 3f). Notably, the cracks in the nanowire and nanoflake coupling layer increased significantly after 5000 bending cycles (Figure 3g and 3h). Similarly, the nanowire and nanoflake still maintain the connection between the cracks after 5000 bending cycles, which demonstrates the good stability and excellent electrical performance of PMAP in repeated cycles (Figure 3i). Here, the SEM images of the Ag layer microstructure also agree well with the resistance response mechanism of PMAP during the mechanical loading and unloading.

Here, the macroscopic and microstructure and morphology of the PMAP actuator were characterized (**Figure 4**). As shown in Figure 4a, the thickness of PMAP actuator is 216.6 μm. Due to the thin U-shape structure of the conductive layer and PI packaging process, only three layers of PMAP actuator can be displayed under optical microscope (Figure 4b). SEM images further shows the cross section microstructure and morphology of PMAP
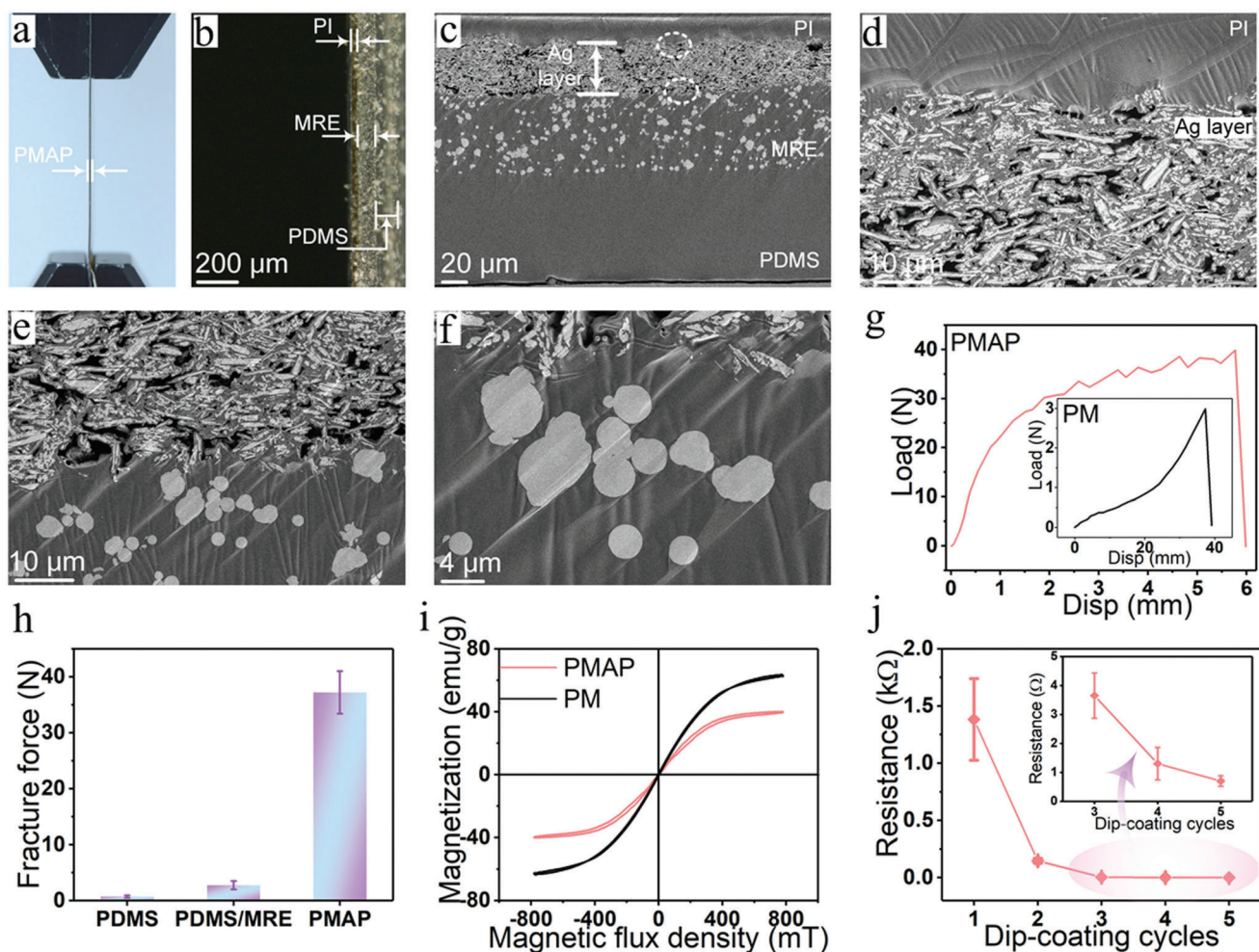
ADVANCED
SCIENCE NEWS
www.advancedsciencenews.com

ADVANCED
MATERIALS
TECHNOLOGIES
www.advmattechnol.de

Figure 4. The section images of a) PMAP actuator and b) the optical microstructure; SEM images of cross section: c) PMAP, d) the magnified view of PI and Ag layer, and e) the enlarged area of Ag layer and MRE; f) SEM image of Carbonyl iron particles (CIPs) in the MRE matrix; g) tensile fracture performance of PMAP and PDMS/MRE (PM); h) the maximum tensile fracture force of PDMS, PM and PMAP; i) saturation magnetization of PMAP and PM; j) resistance of PMAP actuator with different dip-coating cycles.

actuator (Figure 4c–e). As shown in Figure 4c, the thicknesses of PI, Ag layer, MRE and PDMS are 20, 42.5, 66.5, and 87.6 µm, respectively. Clearly, the tight combination of PI and conductive layer ensures the formation of stable multilayer structure (Figure 4d). Moreover, the conductive layer was embedded with the MRE matrix, which made the conductive layer be closely adhered to the substrate (Figure 4e). Therefore, the tightly combined conductive layer ensures good electrothermal effect. Notably, the CIPs were randomly distributed in the MRE matrix (Figure 4f). Due to the excellent magnetic characteristic of the CIPs, the PMAP actuator has a good noncontact magnetic actuated property.

Figure 4g,h shows the tension mechanical performance of PMAP, which demonstrates the tensile fracture force and fracture displacement of PMAP actuator is 39.9 N and 5.7 mm, respectively. Notably, the maximum tensile fracture force of PDMS and PM is 0.7 and 2.8 N, respectively (Figure 4h). Therefore, the PI tape enhanced the mechanical properties of the flexible matrix. Originated from the magnetic CIPs, PMAP actuator shows

a typical soft magnetic effect. The saturation magnetizations of PMAP and PM are 40.5 and 63.7 emu g^{-1}, respectively (Figure 4i). Due to the presence of the conductive Ag layer, the PMAP actuator exhibits a good electrical performance. The effect of dip-coating cycles on electrical properties of PMAP actuator was also researched. As shown in Figure 4j, with increasing of the dip-coating cycles, the mass content of Ag mixture increases, thus the resistance decreases. Notably, the resistance of PMAP actuator is about 0.5 Ω after 5 dip-coating cycles.

2.3. Electric–Thermal Coupling Behavior of the PMAP Actuator

The U-shape PMAP soft actuator with a unique electrothermal characteristic was systematically investigated (**Figure 5**). Figure 5a,b shows the optical images of PMAP actuator and the U-shape Ag layer, respectively. The optical microscope image exhibits the dense distribution of Ag mixture without external mechanical stimulation (Figure 5c). Moreover, SEM image
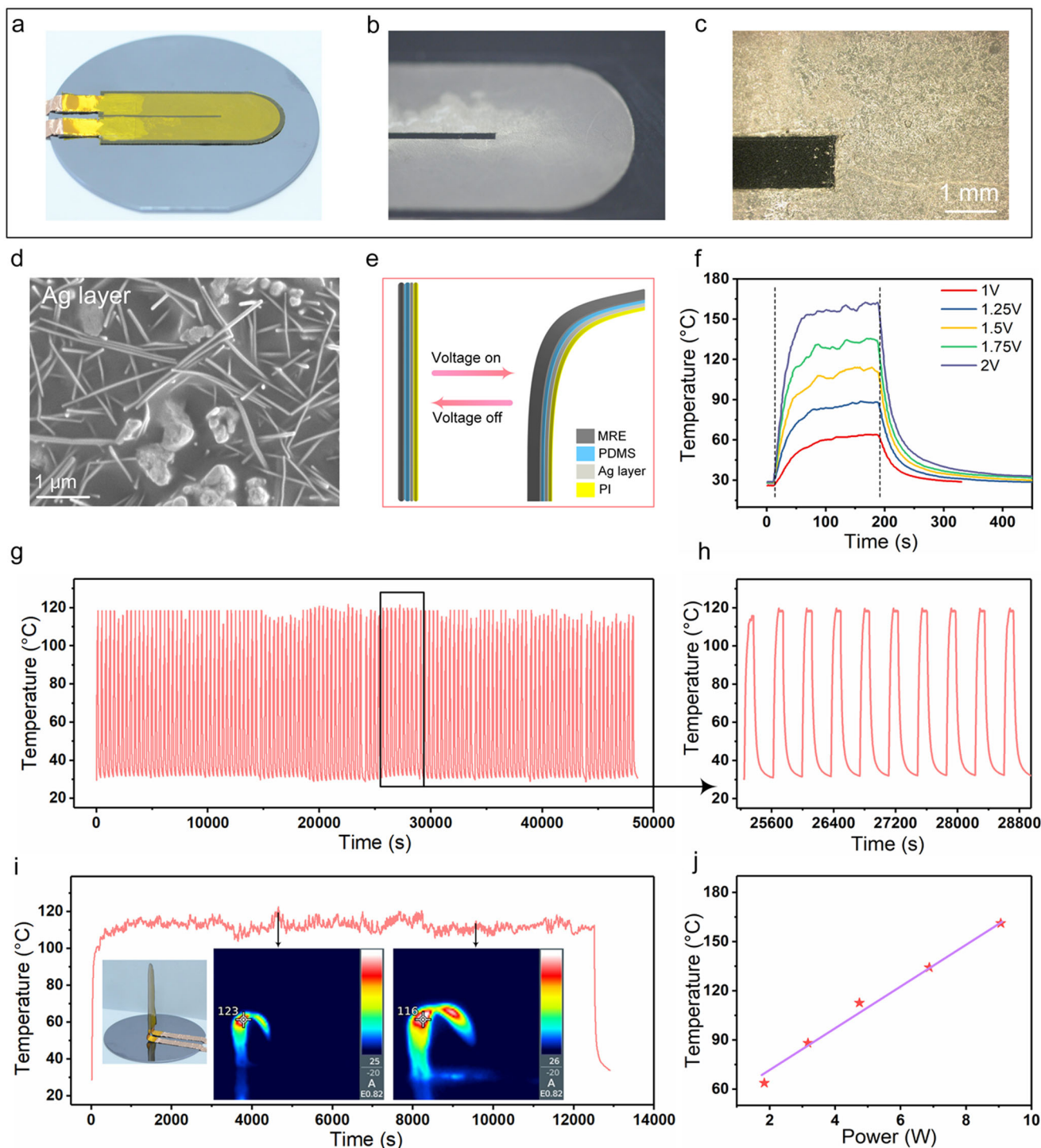
ADVANCED
SCIENCE NEWS

www.advancedsciencenews.com

ADVANCED
MATERIALS
TECHNOLOGIES

www.advmattechnol.de

Figure 5. The images of a) PMAP actuator and b) U-shape Ag layer; c) optical microscope structure of U-shape Ag layer; d) SEM image of Ag layer; e) schematic diagram of PMAP electrothermal actuate; f) time-dependent temperature profiles under different actuating voltage for 180 s; g) cyclic electrothermal stability of PMAP actuator at 1.5 V, h) magnified curve of actuating temperature under 1.5 V; i) temperature stability of PMAP actuator at a constant voltage of 1.5 V for 12000 s; j) experimental results of saturation temperature as a function of electrical power.

ADVANCED
SCIENCE NEWS

www.advancedsciencenews.com

ADVANCED
MATERIALS
TECHNOLOGIES

www.advmattechnol.de

shows the micromorphology of Ag layer. Clearly, the AgNWs and Ag flake assembled to form 3D staggered structure, which endows the PMAP actuator with excellent electrical conductivity (Figure 5d). The actuation of the electrothermal actuator is based on the strain mismatch of two materials with different thermal expansion coefficients when the temperature increases. A good electrothermal soft actuator requires three features: high temperatures under low voltage, excellent heating behavior during the actuating process, and stable materials with a wide temperature range.[28] In this work, the PMAP actuator was consisted of four layer structures with PDMS film, MRE film, Ag layer, and PI tape (Figure 5e). Notably, the nanowire–nanoflake coupling 3D interaction conductive structure was composed of AgNWs and Ag flake with superb conductivity. The temperature of PDMS film and PI tape increased after the conductive circuit was connected, and the contact electrothermal actuate was realized due to the thermal expansion coefficients difference of the PDMS and PI tape.

Figure 5f shows the temperature vs time curves of PMAP actuator under various voltages. The temperature of PMAP increases sharply after the circuit is energized until reaching the steady state temperature, and the temperature decreases rapidly to the room temperature after the circuit is powered off. Moreover, the temperature of PMAP actuator can reach to 116 °C at 1.5 V. After 120 cycles of voltage loading–unloading, PMAP actuator remains stable and repeatable electrothermal performance (Figure 5g). Notably, the SEM images present the microstructure and micromorphology of PMAP actuator do not show any crack and defect (Figure S3a–c, Supporting Information). Additionally, the ten cycles of temperature rising-decreasing indicate the stability of the PMAP actuator (Figure 5h). In order to further evaluate the heating behavior of PMAP, the voltage was kept at 1.5 V to investigate the stability (Figure 5i). The temperature of PMAP actuator was continuously maintained at about 116 °C under the voltage loading over 48000 s, which presented good long-term stability. Moreover, the inset infrared thermal images show the electrothermal actuate deformation and temperature distribution of PMAP actuator. Figure 5j shows the linear fit relationship between the saturation temperature and the applied power. Obviously, the saturation temperature increases with the increasing of applied power, which endows the programmable and controllable deformation capability of PMAP actuator. Therefore, PMAP actuator shows superb stability, good reliability, and repeatability.

2.4. Contact Electrothermal Actuate and Noncontact Magnetic Actuate Behavior

Here, the contact electrothermal actuate and noncontact magnetic actuate performances were systematically investigated (**Figure 6**). Notably, this study developed a new type of MRE with electrothermal–magnetic coupling actuate characteristics. Figure 6a presents schematic diagram of the bending deformation of PMAP actuator at different loading voltages. Moreover, the electrothermal actuate deformation of PMAP actuator at 1, 1.5, and 2 V was investigated (Figure 6b; Movies S1–S3, Supporting Information). The PMAP actuator shows 90° bending deformation under 1 V loading voltage. Additionally, the electrothermal actuate curling deformation of PMAP actuator can be realized

within 16 s under the 2 V loading voltage (Figure 6b). Clearly, the deformation degree of PMAP actuator is strengthened with increasing of the loading voltage. Furthermore, the conductivity of PMAP actuator under electrothermal actuate within different voltages is the vital evaluate factor, which is important for assessing the stability of the soft actuator.

As shown in Figure 6c, the resistance of PMAP under different loading voltages remains almost unchanged, which shows the good stability and excellent conductivity of the PMAP. The infrared thermal inset images exhibit the heat distribution and temperature of PMAP actuator under different voltage. In order to further explore the relationship between the deformation angle and resistance change of the PMAP actuator, the 2 V loading voltage was selected and researched (Figure 6d). Obviously, the resistance of PMAP actuator decreased with increasing of the bending angle. Moreover, the resistance was changed from 0.53 to 0.50 Ω, and the bending angle was 219.3° after 16 s of 2 V voltage loading. Due to the squeezing effect of PMAP actuator during the curling deformation process, the number of contact node between the AgNWs and Ag flake was increased. In this case, the connections in the Ag mixture conductive network became much tighter, and thus the resistance of PMAP actuator was hardly changed under electrothermal actuation. Therefore, the weak resistance change does not affect the electrothermal actuate effect of PMAP actuator.

After investigating the contact electrothermal actuate, the noncontact magnetic actuate performance of PMAP actuator was then explored. Figure 6e shows the schematic diagram of the actuating deformation process of PMAP film under magnetic attraction. Clearly, the deformation degree of PMAP actuator under magnetic field increases with increasing of the magnetic field density (Figure 6f). Here, Movie S4 (Supporting Information) shows the noncontact actuation of PMAP under 28 mT magnetic field density. Notably, the actuating deformation of PMAP film under the magnetic field can be fed back in real time by tracking the resistance change (Figure 6g). Moreover, the electrical signal changed obviously with increasing of the magnetic field density, and the resistance of PMAP film was decreased during the magnetic actuation. The ΔR of PMAP actuator is −0.21 and −0.36 Ω under 28 and 84 mT magnetic field density, respectively. During the magnetic actuate process, the side of Ag layer adhered to the PI tape was under tensile traction, which reduced the conductive contact node. However, a large bending and squeezing effect was occurred on the bonding side of the Ag layer and MRE, which increased the contact nodes of the conductive network, and finally the resistance decreased. At last, the PMAP film exhibits the opposite direction to the electrothermal actuate under magnetic field, and realizes the dual-modal bidirectional actuate.

In order to further investigate and verify the actuating mechanism of PMAP actuator, finite-element method (FEM) was adopted to simulate the deformation characteristics of PMAP actuator (**Figure 7**). The simulation was completed by COMSOL Multiphysics software. Moreover, the geometric model was first designed by SolidWorks software and then directly imported into COMSOL. In the simulation of contact electrothermal actuate, the three physical fields (electric field, thermal field, and solid mechanics) were used for coupling solution in the FEM, and the study type was a steady-state. Notably, the voltage and temperature relationship of PMAP actuator at 1.5 V were firstly
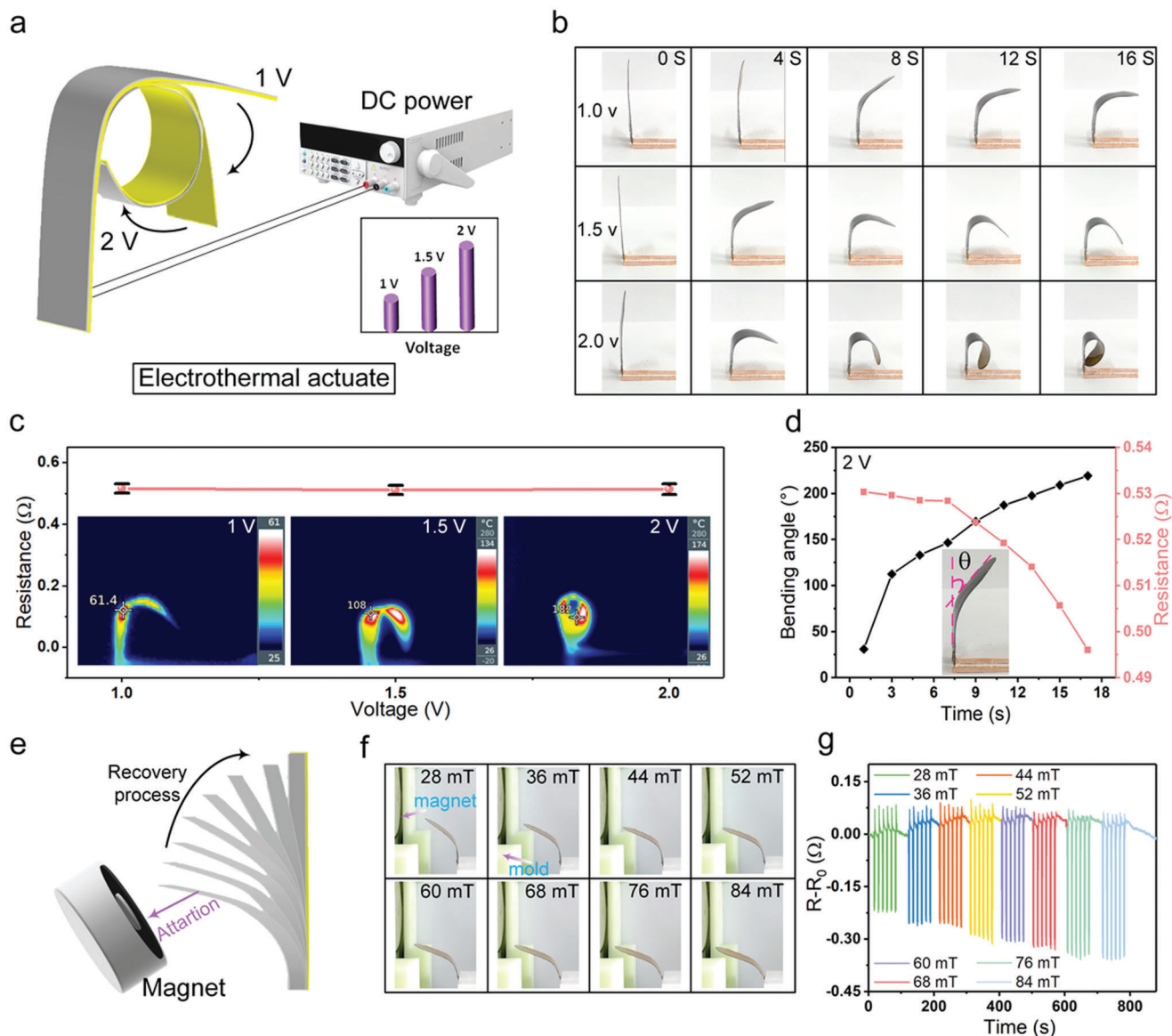
**ADVANCED
SCIENCE NEWS**

www.advancedsciencenews.com

**ADVANCED
MATERIALS
TECHNOLOGIES**

www.advmattechnol.de

Figure 6. a) Schematic diagram of PMAP electrothermal actuate from 1 to 2 V; b) PMAP electrothermal actuate deformation images under different voltages and times; c) resistance and infrared thermal images of PMAP under different voltages; d) PMAP actuator bending angle and resistance vs time at 2 V; e) schematic diagram of the attraction and recovery process of PMAP actuator under magnetic field loading–unloading; f) images of PMAP magnetic actuate and g) magnetic–electric performance of PMAP actuator under different magnetic fields.

calculated, which revealed the distribution of the current direction and the temperature gradient (Figure 7a,b). Figure 7c shows the comparison between the temperature experimental data and simulation results of PMAP actuator. The experiment and simulation result of PMAP actuator at 1.5 V was 116 and 112 °C, respectively. Obviously, the variation trend of the simulation and experimental data was consistent, which indicated the established model could describe the temperature distribution behavior.

Furthermore, the electrothermal actuate of PMAP at 1.25 V (Figure 7d), 1.5 V (Figure 7e), and 1.75 V (Figure 7f) was simulated. Here, due to the limitation of computational convergence, the model could not match the large curling deformation well.

Because of the thermal expansion coefficient difference of PDMS and PI tape, the PMAP film was actuated and its deformation varied significantly with increasing voltage. As a result, the simulation results qualitatively revealed the large deformation of PMAP actuator at various voltages, which provided a theoretical basis for electrothermal actuation experiments. In the simulation of non-contact magnetic actuate, the two physical fields of magnetic field and solid mechanics were used for coupling solution. Figure 7g shows the spatial magnetic field generated by the electromagnet. Notably, the magnetic actuate simulated deformation is in the opposite direction to the electrothermal actuate, and the deflection of PMAP actuator can be actively controlled by adjusting the magnetic field density. Figure 7h–k shows the simulated deformation
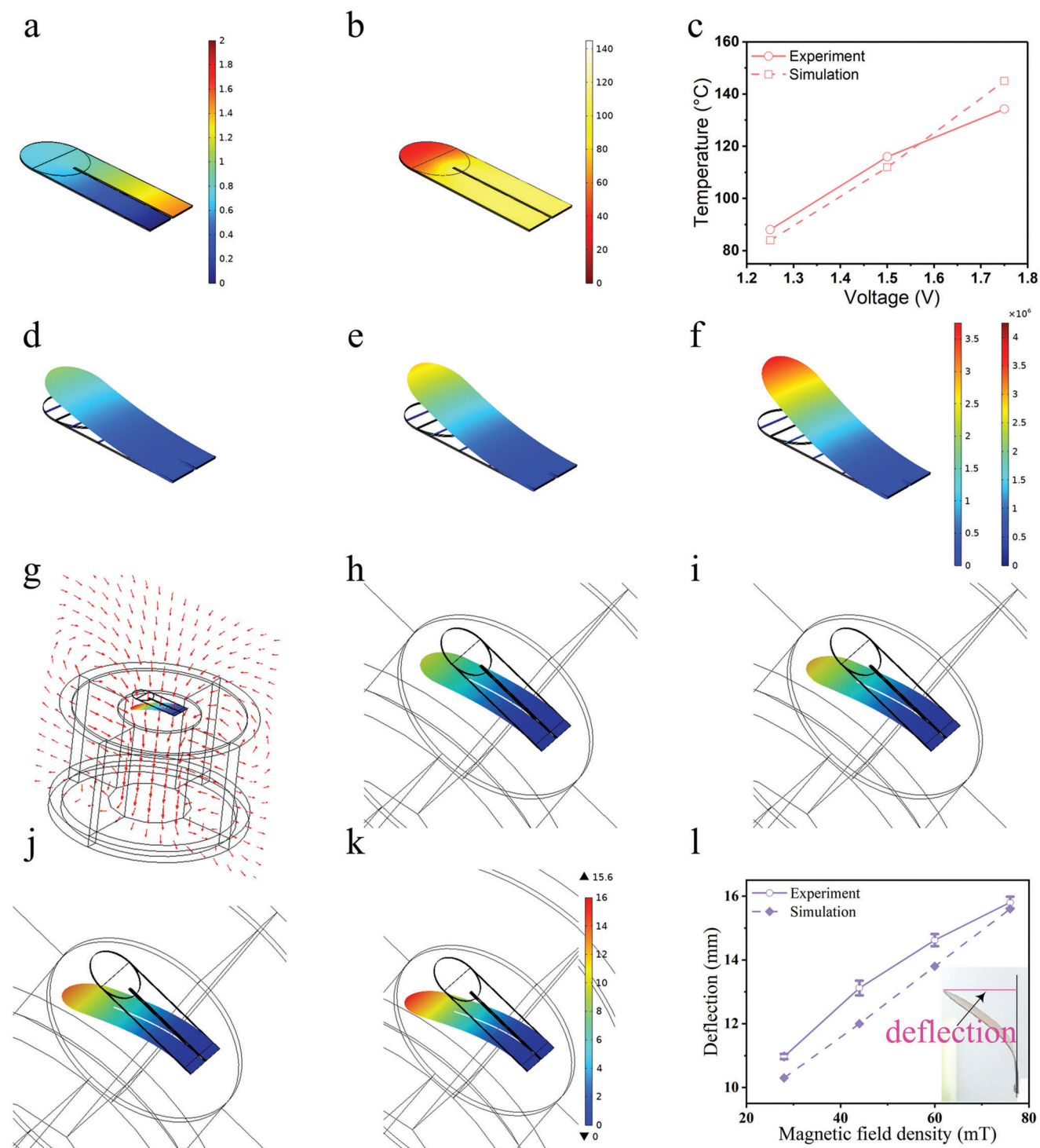
Figure 7. a) Voltage and b) temperature distribution of PMAP actuator at 1.5 V, c) experiment and simulation value of temperature for PMAP actuator. Finite-element simulation of contact electrothermal actuate and noncontact magnetic actuate of PMAP actuator. Different actuating voltage: d) 1.25 V, e) 1.5 V, and f) 1.75 V; g) distribution diagram of magnetic field generated by electromagnet; Different magnetic actuate at h) 28 mT, i) 44 mT, j) 60 mT, and k) 76 mT magnetic field; l) experiment and simulation value of deflection under magnetic actuation of PMAP actuator.
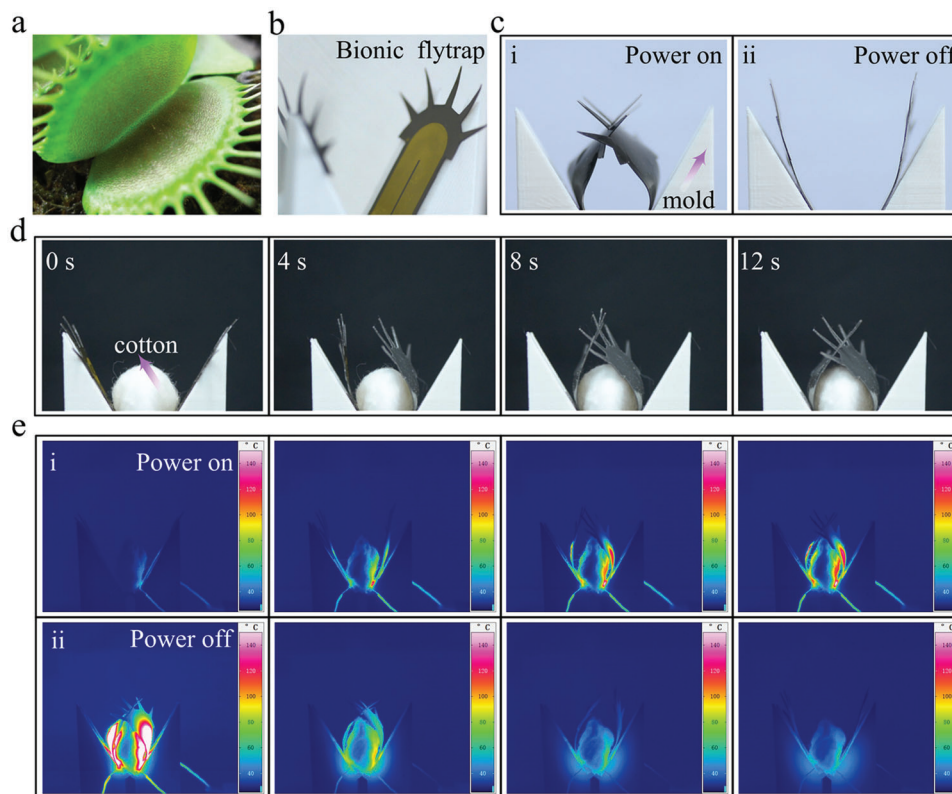
**ADVANCED
SCIENCE NEWS**

www.advancedsciencenews.com

**ADVANCED
MATERIALS
TECHNOLOGIES**

www.advmattechnol.de

Figure 8. The optical image of a) Venus flytrap and b) biomimetic Venus flytrap based on PMAP actuator; c) the closing–opening process of the biomimetic Venus flytrap under the power on–off; electrothermal actuate of cotton capture by biomimetic Venus flytrap: d) the actuation process, e) thermal infrared images under i) power on, and ii) power off.

results of the actuator at 28, 44, 60, and 76 mT magnetic fields, respectively. Clearly, the deformation of PMAP actuator becomes more obvious with increasing of magnetic field density. Moreover, Figure 7l shows the comparison between the experimental data and simulation results of the actuator deflection displacement under different magnetic field. Notably, the error bars indicated that the experimental data were similar to the simulated values after three repeated tests. The experiment and simulation deflection displacement of PMAP actuator at 60 mT was 14.76 and 13.8 mm, respectively. Obviously, the simulation results were similar to the experimental data. As a result, the FEM can qualitatively simulate the bidirectional deformation trend of the actuator, which is consistent with the experiment phenomenon. Therefore, this result can be further applied to guide the structural design of smart soft actuators.

2.5. Electrothermal Actuate Performance of Biomimetic Venus Flytrap

During the past few years, the researches on biomimetic devices based on the soft actuators have attracted extensive attention.[38] The significance of investigating biomimetic devices is to build a bridge between biology and technology to promote the development of artificial intelligence. In this work, the biomimetic Venus flytrap was designed and developed based on the PMAP actua-

tor, which endowed the biomimetic Venus flytrap with characteristics of contact electrothermal actuation. The electrothermal actuate to simulate the predation behavior of Venus flytrap was mainly investigated (**Figure 8**; Movie S5, Supporting Information). Moreover, the bionic flower deformation behavior of the biomimetic actuator was also researched (Figure S4 and Movie S7, Supporting Information). As shown in Figure S4 (Supporting Information), the biomimetic flower was deformed under the electrothermal loading. Notably, the PMAP actuators can be combined with series connection, which greatly facilitates the design of biomimetic devices with different structures and functions.

Different from the natural Venus flytrap (Figure 8a), the biomimetic Venus flytrap was prepared with simplified structure and electrothermal actuate characteristics (Figure 8b). As shown in Figure 8ci, the biomimetic Venus flytrap was closed after power on, and which returned to the initial predatory state after power off (Figure 8c,ii). Furthermore, the cotton was used to vividly demonstrate the closing process of the biomimetic Venus flytrap under electrothermal actuation (Figure 8d). In addition, the infrared thermal images were well displayed the process of closure and opening of biomimetic Venus flytrap (Figure 8e; Movie S6, Supporting Information). Notably, the high temperature of 130°C generated by the biomimetic Venus flytrap during the closure process is fatal to the prey. Here, the soft actuator based on electrothermal actuate expands the research direction for investigating the multimodal actuate mode and application

**ADVANCED
SCIENCE NEWS**

www.advancedsciencenews.com

**ADVANCED
MATERIALS
TECHNOLOGIES**

www.advmattechnol.de

environment of biomimetic devices. Therefore, this work promotes the development of customized and diversified intelligent biomimetic devices.

3. Conclusions

In summary, a smart soft actuator with self-sensing and dual-modal actuating performances was integrated by using mask-patterning and spin-coating technology, which presented outstanding electric–mechanic–magnetic–thermal coupling response, excellent flexibility, and ultrahigh stability properties. Notably, the PMAP film shows good sensing ability, and the $\Delta R/R_0$ of PMAP film reached to 24.6% and 26.6% when the bending displacement was 20 mm and compression displacement was 0.3 mm, respectively. Moreover, the nanowire–nanoflake coupling conductive Ag layer endowed the PMAP film with the contact electrothermal actuation and noncontact magnetic actuation. Additionally, the bending angle of PMAP film was 219.3° within 16 s under 2 V voltage loading. Furthermore, the PMAP actuator can be continuously energized for 48 000 s to keep the temperature at 116 °C, which demonstrates good thermal stability. The PMAP actuator shows noncontact actuating mode under magnetic field, and the actuating deformation response of PMAP increases with increasing of the magnetic field strength. In order to further research the actuation and deformation of bionic device, the biomimetic Venus flytrap was designed and fabricated based on the PMAP actuator. Here, the PMAP film is promising to be employed as a smart soft actuator.

4. Experimental Section

Materials: The PDMS (type Sylgard 184) precursor and curing agent were supplied from Dow Corning GmbH, USA. Carbonyl iron particles (CIPs, type CN) with an average diameter of 3.85 μm from BASF were used as ferromagnetic particles. The raw materials for self-prepared silver nanowires (AgNWs) solution[37] contained Polyvinylpyrrolidone (PVP), AgNO$_3$, glycerol, and NaCl were from Sinopharm Chemical Reagent Co., Ltd. Silver (Ag) flakes was purchased from Shanghai Sigma High Technology Co., Ltd., China. The polyimide (PI) tape was commercially available product, China.

Fabrication of Multilayer Soft Actuator: Here, the U-shape pattern designed and optimized by CAD software was used to prepare the actuator and sensor with high deformation and good response. The reusable masking films were obtained by hollowing out the commercial polyethylene terephthalate film into the designed pattern via laser cutting technology (Figure S1, Supporting Information).

The curing ratio of PDMS precursor was 20:1. MRE precursor (PDMS curing ratio of 20:1, CIPs mass fraction of 50 wt%) was prepared by stirring the mixture and vacuuming for 5 min. First, PDMS precursor was poured onto a silicon (Si) wafer, spin-coated at 500 rpm for 15 s and 1500 rpm for 15 s, and placed in the oven at 90 °C for 10 min to complete curing. Then, MRE precursor was poured onto the cured PDMS layer, spin-coated at 500 rpm for 15 s and 1500 rpm for 30 s, cured at 90 °C for 3 min with the semicured state. The 10 mL AgNWs (concentration: 8.7 mg mL^{-1}) and 0.4 g Ag flakes were sonicated for 30 min to obtain the conductive Ag mixture.

Then, the masking film was attached to the semicured MRE film. The Ag mixture was coated on the U-shape path and dried on the plate at 35 °C for 5 min, and the conductive Ag layer was formed by repeating the coating operation five times. After that, the PDMS/MRE/Ag layer was cured at 90 °C for 10 min, and the masking film was peeled off after the curing. The wires were adhered to the electrode zones of conductive Ag layer by silver paste. At last, the PI tape was attached to the Ag layer, and the PMAP (PDMS/MRE/Ag layer/PI) multilayer soft actuator was developed. The PMAP actuator was released from the silicon wafer by manual peeling (Figure 1a). In addition, the conductive layer of the PMAP sensor was designed as the strip-shaped pattern.

Characterization: The microstructures of the Ag layer and PMAP were observed by scanning electron microscope (SEM, Philips of Holland, model XL30 ESEM-TMP) under 3 kV. The bending and compression test system consists of a dynamic mechanical analyzer (DMA, Electro-Force 3200, TA instruments, Minnesota 55344 USA) and Modulab MTS (Solartron analytical, AMETEK advanced measurement technology, Inc., United Kingdom). The hysteresis loops of PDMS/MRE (PM) and PMAP were tested by Hysteresis Measurement of Soft and Hard Magnetic Materials (HyMDC Metis, Leuven, Belgium). The electrothermal actuation was performed by a DC power with different voltages. The magnetically responsed response tests were finished by Modulab MTS with a DC power electromagnetic coil. X-ray photoelectron spectroscopy (XPS) of the AgNWs and Ag layer were detected on the X-ray photoemission spectrophotometer (ESCALAB250A, Thermo-VG Scientific, UK). The X-ray diffractometer (Smartlab, Rigaku, Japan) was used to record the X-ray diffraction (XRD) pattern of the AgNWs, Ag flake and Ag layer. The infrared thermal camera (type Image IR 8300, Germany) was used to obtain the thermal actuate images.

Supporting Information

Supporting Information is available from the Wiley Online Library or from the author.

Conflict of Interest

The authors declare no conflict of interest.

Data Availability Statement

Research data are not shared.

[1] L. Ding, S. H. Xuan, J. B. Feng, X. L. Gong, *Composites, Part A* **2017**, *100*, 97.

[2] S. J. Paul, I. Elizabeth, B. K. Gupta, *ACS Appl. Mater. Interfaces* **2021**, *13*, 8871.

[3] Z. Tang, Z. Gao, S. Jia, F. Wang, Y. Wang, *Adv. Sci.* **2017**, *4*, 1600437.

[4] L. Lu, D. Zhang, Y. Xie, H. He, W. Wang, *Adv. Mater. Technol.* **2022**, *7*, 2200441.

[5] P. Li, Y. Zhao, J. Ma, Y. Yang, H. Xu, Y. Liu, *Adv. Mater. Technol.* **2020**, *5*, 1900823.

[6] J. Peng, H. Zhang, Q. Zheng, C. M. Clemons, R. C. Sabo, S. Gong, Z. Ma, L. S. Turng, *Nanoscale* **2017**, *9*, 1428.

[7] S. Peng, P. Blanloeuil, S. Wu, C. H. Wang, *Adv. Mater. Interfaces* **2018**, *5*, 1800403.

[8] D. Wang, X. Zhou, R. Song, C. Fang, Z. Wang, C. Wang, Y. Huang, *Chem. Eng. J.* **2021**, *404*, 126940.

[9] M. Sang, G. Liu, S. Liu, Y. Wu, S. H. Xuan, S. Wang, S. Y. Xuan, W. Q. Jiang, X. L. Gong, *Chem. Eng. J.* **2021**, *414*, 128883.

[10] P. Zhou, J. Lin, W. Zhang, Z. Luo, L. Chen, *Adv. Sci.* **2022**, *9*, 2104270.

[11] W. Liao, Z. Yang, *Adv. Mater. Technol.* **2022**, *7*, 2101260.

[12] H. Li, Y. Liang, G. Gao, S. Wei, Y. Jian, W. Le, W. Lu, Q. Liu, J. Zhang, T. Chen, *Chem. Eng. J.* **2021**, *415*, 128988.

[13] Y. Qiu, C. Wang, X. Lu, H. Wu, X. Ma, J. Hu, H. Qi, Y. Tian, Z. Zhang, G. Bao, H. Chai, J. Song, A. Liu, *Adv. Funct. Mater.* **2022**, *32*, 2110296.

[14] N. Chen, Y. Zhou, Y. Liu, Y. Mi, S. Zhao, W. Yang, S. Che, H. Liu, F. Chen, C. Xu, G. Ma, X. Peng, Y. Li, *Nano Res.* **2022**, *15*, 7703.

[15] Y. Zhao, C. Y. Lo, L. Ruan, C. H. Pi, C. Kim, Y. Alsaid, I. Frenkel, R. Rico, T. C. Tsao, X. He, *Sci. Robot.* **2021**, *6*, eabd5483.

[16] Q. Shu, Z. B. Xu, S. Liu, J. P. Wu, H. X. Deng, X. L. Gong, S. H. Xuan, *Chem. Eng. J.* **2022**, *433*, 134424.

[17] B. Liu, C. L. Yuan, H. L. Hu, H. Wang, Y. W. Zhu, P. Z. Sun, Z. Y. Li, Z. G. Zheng, Q. Li, *Nat. Commun.* **2022**, *13*, 2712.

[18] S. Yang, Y. He, Y. Liu, J. Leng, *Composites, Part A* **2022**, *158*, 106940.

[19] S. Taccola, F. Greco, E. Sinibaldi, A. Mondini, B. Mazzolai, V. Mattoli, *Adv. Mater.* **2015**, *27*, 1668.

[20] Q. Ze, X. Kuang, S. Wu, J. Wong, S. M. Montgomery, R. Zhang, J. M. Kovitz, F. Yang, H. J. Qi, R. Zhao, *Adv. Mater.* **2020**, *32*, 1906657.

[21] K. Ni, Q. Peng, E. Gao, K. Wang, Q. Shao, H. Huang, L. Xue, Z. Wang, *ACS Nano* **2021**, *15*, 4747.

[22] Z. Ren, W. Hu, X. Dong, M. Sitti, *Nat. Commun.* **2019**, *10*, 2703.

[23] Y. Yang, Y. Liu, Y. Shen, *Adv. Funct. Mater.* **2020**, *30*, 1910172.

[24] M. Leveille, X. Shen, W. Fu, K. Jin, M. Acerce, C. Wang, J. Bustamante, A. M. Casas, Y. Feng, N. H. Ge, L. S. Hirst, S. Ghosh, J. Q. Lu, *Adv. Sci.* **2021**, *8*, 2102077.

[25] Z. Chen, Y. Chen, C. Chen, X. Zheng, H. Li, H. Liu, *Chem. Eng. J.* **2021**, *424*, 130562.

[26] K. Dai, Z. Zhu, H. Jin, X. Ma, W. Duan, J. Wang, W. Zhang, *Adv. Mater. Interfaces* **2022**, *9*, 2200351.

[27] S. Jiang, W. Guo, S. Liu, X. Huang, Y. Li, Z. Li, H. Wu, Z. Yin, *ACS Appl. Mater. Interfaces* **2019**, *11*, 47476.

[28] W. W. Li, M. Sang, S. Liu, B. C. Wang, X. F. Cao, G. H. Liu, X. L. Gong, L. Y. Hao, S. H. Xuan, *Composites, Part B* **2022**, *238*, 109880.

[29] B. Zhu, H. Wang, Y. Liu, D. Qi, Z. Liu, H. Wang, J. Yu, M. Sherburne, Z. Wang, X. Chen, *Adv. Mater.* **2016**, *28*, 1559.

[30] W. Zhou, S. Yao, H. Wang, Q. Du, Y. Ma, Y. Zhu, *ACS Nano* **2020**, *14*, 5798.

[31] S. Cho, D. h. Kang, H. Lee, M. P. Kim, S. Kang, R. Shanker, H. Ko, *Adv. Sci.* **2021**, *8*, 2001647.

[32] Y. Jiang, K. Dong, X. Li, J. An, D. Wu, X. Peng, J. Yi, C. Ning, R. Cheng, P. Yu, Z. L. Wang, *Adv. Funct. Mater.* **2021**, *31*, 2005584.

[33] H. Kang, C. Zhao, J. Huang, D. H. Ho, Y. T. Megra, J. W. Suk, J. Sun, Z. L. Wang, Q. Sun, J. H. Cho, *Adv. Funct. Mater.* **2019**, *29*, 1903580.

[34] K. Zhou, Y. Zhao, X. Sun, Z. Yuan, G. Zheng, K. Dai, L. Mi, C. Pan, C. Liu, C. Shen, *Nano Energy* **2020**, *70*, 104546.

[35] Q. Gao, B. A. F. Kopera, J. Zhu, X. Liao, C. Gao, M. Retsch, S. Agarwal, A. Greiner, *Adv. Funct. Mater.* **2020**, *30*, 1907555.

[36] M. Piedrahita-Bello, Y. Zan, A. Enriquez-Cabrera, G. Molnár, B. Tondu, L. Salmon, A. Bousseksou, *Chem. Phys. Lett.* **2022**, *793*, 139438.

[37] C. Yang, H. Gu, W. Lin, M. M. Yuen, C. P. Wong, M. Xiong, B. Gao, *Adv. Mater.* **2011**, *23*, 3052.

[38] X. F. Cao, S. H. Xuan, S. S. Sun, Z. B. Xu, J. Li, X. L. Gong, *ACS Appl. Mater. Interfaces* **2021**, *13*, 30127.